Vibrational relaxation and decoherence of Rb_2 attached to helium nanodroplets

B. Grüner[1], M. Schlesinger[2], Ph. Heister[1] , W. T. Strunz[2], F. Stienkemeier[1], M. Mudrich[1]
[1] *Physikalisches Institut, Universität Freiburg, 79104 Freiburg, Germany and*
[2] *Institut für Theoretische Physik, Technische Universität Dresden, 01062 Dresden, Germany*
(Dated: November 4, 2010)

The vibrational wave-packet dynamics of diatomic rubidium molecules (Rb_2) in triplet states formed on the surface of superfluid helium nanodroplets is investigated both experimentally and theoretically. Detailed comparison of experimental femtosecond pump-probe spectra with dissipative quantum dynamics simulations reveals that vibrational relaxation is the main source of decoherence. The rate constant for vibrational relaxation in the first excited triplet state $1^3\Sigma_g^+$ is found to be constant $\gamma \approx 0.5\,\mathrm{ns}^{-1}$ for the lowest vibrational levels $v \lesssim 15$ and to increase sharply when exciting to higher energies.

I. INTRODUCTION

Helium nanodroplet isolation (HENDI) is a well-established technique for isolating molecules and forming clusters at low temperature (0.38 K) for spectroscopic studies [1]. Shifts and broadenings of spectral lines of molecules embedded in the helium droplets are small due to the weak dopant-host interactions as well as to the peculiar quantum properties of the superfluid helium nanodroplets [2, 3]. Nevertheless, the details of the solute-solvent interactions that are at the origin of the observed line shapes are currently being studied with various approaches [4–8]. However, to date no time-resolved studies aiming at resolving the details of the interaction of excited molecules with helium nanodroplets have been performed.

Vibrational relaxation of molecules and molecular complexes embedded in helium nanodroplets has been studied by the group of R. Miller using high-resolution infrared spectroscopy and bolometric detection [4, 9–11]. It was found that systems having a large energy gap between the molecular vibration and the excitations of the helium (*e. g.* HF ($v = 1$)) couple very inefficiently to the helium environment, which leads to slow vibrational relaxation times $t \gtrsim 0.5\,\mathrm{ms}$. The observed droplet-size dependent line shifts and broadenings point at coupling to surface excitations of the helium droplets (ripplons) being the main mechanism of relaxation [11]. Using microwave spectroscopy, droplet-size dependent rotational relaxation times have been determined to be of order 1 – 10 ns [5].

Recently, experiments have been performed that probe the dynamics of spin relaxation, dissociation, aggregation, exciplex formation, and vibration of molecules attached to helium nanodroplets [12–20]. These studies have in common that the helium nanodroplets act as a dissipative environment that decisively affects the outcome and the dynamics of the process of interest. Therefore, the dynamics of cooling, relaxation and decoherence induced by the ultracold bath of helium atoms attracts an increasing amount of attention from both experiment and theory.

The vibrational wave packet dynamics of alkali metal dimers attached to helium nanodroplets has been studied using the femtosecond pump-probe technique in a series of experiments in our group [3, 12, 19, 20]. Alkali metal atoms and molecules represent a particular class of dopant particles due to their extremely weak binding to the surface of He droplets in bubble-like structures [21–24]. In particular pump-probe measurements with K_2 diatomic molecules in singlet states attached to helium droplets reveal a significant impact of the helium environment on the vibrational dynamics, suggesting the manifestation of a Landau critical velocity for the vibrational motion of K_2 on the surface of superfluid helium nanodroplets [19, 25].

In this work we present the detailed analysis of pump-probe measurements of the vibrational wave packet dynamics of Rb_2 molecules in triplet states attached to helium nanodroplets with regard to relaxation and decoherence induced by the helium environment. This system is particularly well-suited for a quantitative study of the molecule-helium droplet interaction due to the precise knowledge of the spectra and dynamics of gas-phase Rb_2 molecules and due to the weak molecule-helium interactions which allow for an accurate theoretical description.

The long-lasting wave packet oscillations that we observe up to delay times $t \gtrsim 1.5\,\mathrm{ns}$ suggested that the Rb_2 molecules desorb off the helium droplets on a short time scale $t \lesssim 10\,\mathrm{ps}$ and continue to vibrate freely in the gas-phase [12]. This assumption was backed by the good agreement between the measured and theoretically predicted vibrational frequencies. Besides, the measurement of beam depletion using a separate detector was interpreted as clear evidence that excited Rb_2 molecules desorb off the droplets on the time scale of the flight time from the laser interaction region to the detector ($\sim 1\,\mathrm{ms}$). Furthermore, earlier measurements with K_2 dimers as well as theoretical simulations on K atoms attached to helium nanodroplets indicated desorption times in ranging 3 – 8 ps and 10 – 30 ps, respectively [19, 26].

A more detailed inspection of our data reveals, however, that the Rb_2 molecules are subject to continuous vibrational relaxation due to the constant coupling to the bath of helium atoms on the time scale of the pump-probe measurements. The experimental signature of the coupling of vibrating Rb_2 to the helium is the decreas-

ing contrast of wave packet oscillation signals as well as changing amplitudes of individual Fourier frequency components due to the redistribution of populations of vibrational states. In particular, the pronounced dependence of the dephasing time on the quantum number v of excited vibrational levels points at system-bath couplings being active. This observation is in line with earlier measurement of the fluorescence emissions of Na_2 atoms in triplet states, which indicated vibrational relaxation in the excited electronic state to take place on the time scale of the life time of the excited state due to spontaneous emission ($\sim 10\,$ns) [27]. Recently, it was observed that desorption upon electronic excitation may even be completely inhibited in the case of Rb atoms excited in a particular laser wave length range [28].

Pioneering experiments on the vibrational decoherence and relaxation of molecules (I_2) exposed to collisions with rare gas atoms at high density were performed by the Zewail group [29], motivating theoretical studies by Engel, Meier *et al.* [30, 31]. More recently, decoherence times as well as relaxation rates have been studied extensively by the groups of Apkarian and Schwentner by means of femtosecond spectroscopy of the vibrational dynamics of halide molecules isolated in cryogenic rare-gas matrices [32–37]. However, to the best of our knowledge, no time-resolved measurements of the molecular dynamics in bulk superfluid helium has been reported so far.

Theoretical studies on collisional quenching of rotations and vibrations of alkali dimers and other small molecules by helium atoms at low temperatures have recently been stimulated by the prospects of creating samples of cold molecules using buffer-gas cooling as well as sympathetic cooling with ultracold atoms as a cooling agent [38–40]. In the system Li_2+He, for instance, the quenching rate constants in the approximation of vanishing temperature are predicted to increase by about one order of magnitude with increasing vibrational levels $v = 0 - 10$ [38].

In the case of weak couplings, which applies to our system, the concept of perturbations of the vibrational levels of the molecules by fluctuations in the bath modes is well-established. The resulting fluctuations of the potential energy and equilibrium coordinate lead to decaying vibrational coherence with time constant T_2 due to vibrational energy relaxation with T_1 as well as due to pure decoherence with T_*. In the low temperature-limit, $T \to 0$, however, the latter contribution vanishes [41, 42]. In the related energy gap picture the populations of individual vibrational energy levels v relax stepwise to the next lower vibrational energy levels $v - 1$ [43]. Here, the relaxation rate for an isolated vibrational level increases with the vibrational quantum number v [35, 42, 44]. The evolution of coherences and populations of vibrational levels in the weak-coupling limit is often being modeled with the master equation description of anharmonic oscillators coupled to a harmonic bath. Various coupling terms are used for describing different interaction mechanisms [35, 42, 45–47].

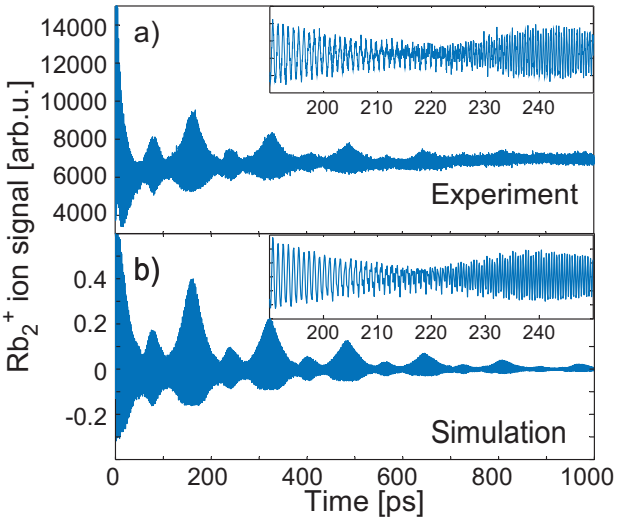

FIG. 1. Experimental (a) and simulated (b) pump-probe transients of Rb_2 formed on helium nanodroplets recorded at the laser wave length $\lambda = 1006\,$nm.

II. VIBRATIONAL WAVE PACKET DYNAMICS

The experimental arrangement used for recording femtosecond pump-probe photoionization transients is identical to the one described previously [12]. In short, a continuous beam of helium nanodroplets of the size of about 8000 He atoms is produced by expanding high-purity ^{4}He gas out of a cold nozzle (T$\approx 17\,$K, diameter $d = 5\,\mu$m) at high pressure (p$\approx$50 bar). The helium droplets are doped with two Rb atoms on average per droplet by passing through a pick-up cell that contains Rb vapor at a pressure $p_{Rb} \approx 2 \times 10^{-4}\,$mbar. Alkali atoms and molecules are peculiar dopants in that they reside in bubble-like structures on the surface of He droplets. Upon formation of a Rb_2 diatomic molecule, the binding energy is dissipated by evaporation of helium atoms from the droplets and occasionally by desorption off the droplets of the newly formed molecule itself. This leads to an enrichment of droplet-bound Rb_2 molecules in weakly bound triplet states.

Further downstream, the doped He droplet beam intersects the laser beam inside the detection volume of a commercial quadrupole mass spectrometer. Due to the limited mass range, only bare Rb_2^+ photoions are detected mass-selectively. The laser beam consists of pairs of identical pulses produced by a commercial mode-locked Ti:sapphire laser and a Mach-Zehnder interferometer to adjust the time delay between the pulses. The pulses have a duration of $\approx 160\,$fs and a spectral bandwidth at half maximum of $\Delta\omega_{las} \approx 80\,\mathrm{cm}^{-1}$ and peak pulse intensity $\sim 4\,\mathrm{GW/cm}^2$.

A pronounced oscillatory photoionization signal is observed in the pump-probe transients for laser wave

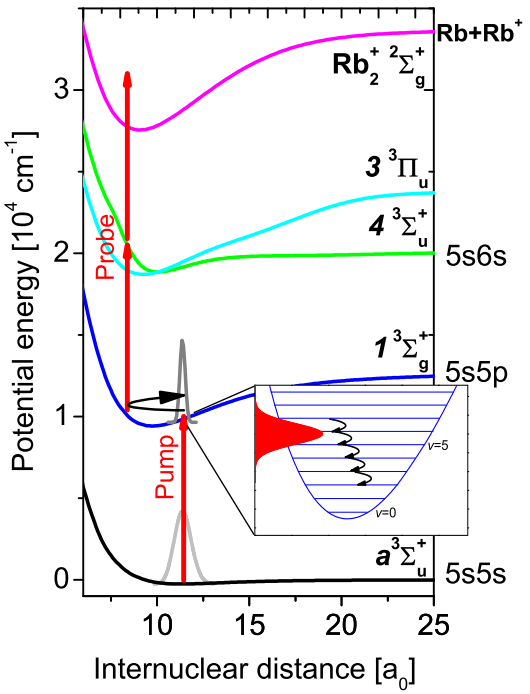

FIG. 2. (Color online) Selected triplet potential-energy curves of neutral Rb_2 and of the Rb_2^+ ionic ground state relevant to the present study. The arrows indicate the creation of a vibrational wave packet in the first-excited state followed by resonant two-photon ionization.

lengths in the range $\lambda = 960\,\mathrm{nm}$ – $1032\,\mathrm{nm}$. A typical measured pump-probe transient recorded at $\lambda = 1006\,\mathrm{nm}$ is depicted in Fig. 1 (a). On the time scale of picoseconds, the transient signal is modulated by wave packet (WP) oscillations with a period $T_{\Sigma g} \approx 0.95\,\mathrm{ps}$ (see inset). In addition, this oscillation is amplitude- and frequency-modulated due to dispersion and subsequent revivals of the WP motion in an anharmonic potential. On the long time scale of hundreds of ps, the contrast of WP oscillations degrades monotonically and eventually vanishes at delay times $\gtrsim 1\,\mathrm{ns}$. This slow decay of coherence is attributed to the effect of decoherence due to the coupling of the Rb_2 molecules to the helium droplets and will be studied in detail in this article.

A. Free gasphase dynamics

Let us first briefly review the fundamental aspects of pump-probe spectroscopy of diatomic molecules isolated in the gas-phase. A first pump pulse excites a coherent superposition of vibrational states (WP) in an excited electronic state. After some time delay a second probe pulse projects the WP to a final ionic state which is detected as a function of time delay between the two pulses. Fig. 2 shows the relevant potential energy curves of the Rb_2 molecule in the triplet manifold. The straight arrows symbolize the pump and probe pulse excitation pathways.

Due to the cold helium environment, at time $t = 0$ only the vibrational ground state on the lowest triplet state $a^3\Sigma_u^+$ is occupied. Experimental data reveal that rotational degrees of freedom need not be taken into account (Sec. III). As outlined in Sec. II C, we fully solve the time-dependent Schrödinger equation involving all relevant potential energy surfaces. Here, we want to point out that the main effect of the pump pulse is to generate a coherent superposition of vibrational eigenstates $|v\rangle$ on the excited electronic state surface $(1)^3\,\Sigma_g^+$. More specifically, the created WP can be written as $|\psi_e(t=0)\rangle = \sum_{v=0}^{N} c_v\,|v\rangle$, where c_v denotes complex expansion coefficients and $v = 0, 1, 2, \ldots$ is the vibrational quantum number. Coherent WPs will also be created in higher lying electronic states or, by resonant impulsive stimulated Raman scattering (RISRS) in the triplet ground state, with a significantly smaller amplitude, though [48]. Thus, all linear and nonlinear processes are fully taken into account in our simulations. The respective populations of vibrational levels $|c_v|^2$ depend on the pump pulse parameters and on the Franck-Condon factors of the excitation transition. The pump pulse wave length determines the central vibrational level, while the pulse width, the pulse energy and the Franck-Condon factors determine the number and the relative populations of vibrational levels. The created WP in the $(1)^3\,\Sigma_g^+$-state propagates in the region between the classical inner and outer turning points. Direct integration of the Schrödinger equation $i\hbar\partial_t\,|\psi_e\rangle = H_e\,|\psi_e\rangle$ yields

$$|\psi_e\,(t)\rangle = \sum_{v=0}^{N} c_v e^{-\frac{\mathrm{i}E_v t}{\hbar}}\,|v\rangle\,, \tag{1}$$

where E_v is the energy of the v-th vibrational level. As discussed below, the measured signal allows to extract information about the density matrix of vibrational states $\rho_e(t)$. For the isolated dimer, $\rho_e(t) = |\psi_e(t)\rangle\langle\psi_e(t)|$ describes a pure state at all times. Its time evolution is given by

$$\rho_e\,(t) = \sum_{v,v'} c_v c_{v'}^* e^{-\frac{i(E_v - E_{v'})t}{\hbar}}\,|v\rangle\,\langle v'|\,. \tag{2}$$

The diagonal elements of the density matrix $\rho_{vv} = |c_v|^2$ represent the populations that are constant in time, while the off-diagonal elements $\rho_{vv'}(t) \equiv \langle v|\rho_e(t)|v'\rangle$ with $v \neq v'$ oscillate with Bohr frequencies $\omega_{vv'} = (E_v - E_{v'})/\hbar$ and represent the coherences between the vibrational eigenstates $|v\rangle$, $|v'\rangle$.

The probe pulse produces photoions through a resonant 2-photon-transition from the excited state to the ionic ground state $^2\Sigma_g^+$ of Rb_2^+. Transitions preferably

take place when the WP is located around a well-defined transition region, where the transition dipole matrix element is maximal (Franck-Condon window). Even though our simulations are numerically exact, it is instructive to consider the perturbative dependence of the ion signal on the WP density matrix [49–52],

$$S(t) = \sum_{vv'} A_{vv'} \rho_{vv'}(t). \tag{3}$$

The coefficients $A_{vv'}$ in Eq. (3) contain products of transition moments and field parameters and provide information about the vibrational populations in the final state. Through the dependence on the density matrix, the signal S is composed of beat frequencies $\omega_{vv'}$ between all pairs of energy levels that contribute to the WP. The most prominent oscillation in the signal originates from components ω_{vv+1} and reflects the circulation of the WP on the potential energy surface. From the Fourier spectra of the signal information about higher-order frequency components $\omega_{vv+\Delta v}$ with $\Delta v > 1$ can be extracted. In this way it is possible to gain information about the density matrix from the measured ion signal.

In a harmonic potential with energy levels $E_n = \hbar\omega_e n$, where $n = 0, 1, 2, \ldots$ denotes the number of eigenstate $|n\rangle$, Eq. (1) yields a periodic oscillation with classical period $T_c = h/\Delta E = 2\pi/\omega_e$, where ΔE denotes the constant energy spacing between adjacent levels n. The signal S in Eq. (3) features a sinusoidal oscillation with period T_c. In the anharmonic Morse potential with energy spectrum $E_v = \hbar\omega_e(v - x_e v^2)$, however, initially well-localized WPs spread out due to dispersion on the characteristic time scale $T_{\mathrm{disp}} = \hbar\hat{\omega}/(\omega_e x_e \Delta E_{\mathrm{pump}})$ [32, 53, 54]. Here, x_e is the anharmonicity constant, $\hat{\omega}$ denotes the central vibrational frequency of the WP and ΔE_{pump} is the spectral energy width of the pump laser pulse. Considering the parameters of our experiment we obtain $T_{\mathrm{disp}} \sim 100\,\mathrm{ps}$. Around $t = T_{\mathrm{disp}}$, all contributions on the right-hand side of Eq. (3) appear uncorrelated, which means that the oscillatory signal collapses [55]. Therefore, dispersion of the WP leads to a decay of the pump-probe signal contrast. Note, however, that due to dispersion neither populations ρ_{vv} nor the absolute values of coherences $|\rho_{vv'}|$, $v \neq v'$, change in time.

In the Morse potential, a revival of the initial WP takes place at certain times, i. e. the original phase correlation in the WP is restored and the WP partly or fully revives. At the full revival time, the signal amplitude ideally reaches its initial height, which underlines that coherence is preserved. Full revivals occur at times $t = k \times T_{\mathrm{rev}}/2$, where $T_{\mathrm{rev}} = 2\pi/(\omega_e x_e)$, when all vibrational eigenstates have accumulated a phase of $2\pi k$ with $k = 1, 2, 3, \ldots$. At fractions of the revival time, $t = p/q \times T_{\mathrm{rev}}$ where p/q is an irreducible fraction of integers, the WP consists of a superposition of q copies of the original WP (fractional revivals) [56, 57]. For instance, at half-period revivals ($p/q = 1/2$) the initial well-localized WP evolves into a highly quantum mechanical state that consists of two counter-propagating partial WPs that interfere with each other when colliding. In the electronic state of relevance for the present analysis, $1^3\Sigma_g^+$ of Rb_2, which perfectly matches the shape of the Morse potential in the accessible range of v-states, the first full revival time is $T_{\mathrm{rev}}/2 \approx 160\,\mathrm{ps}$ [12].

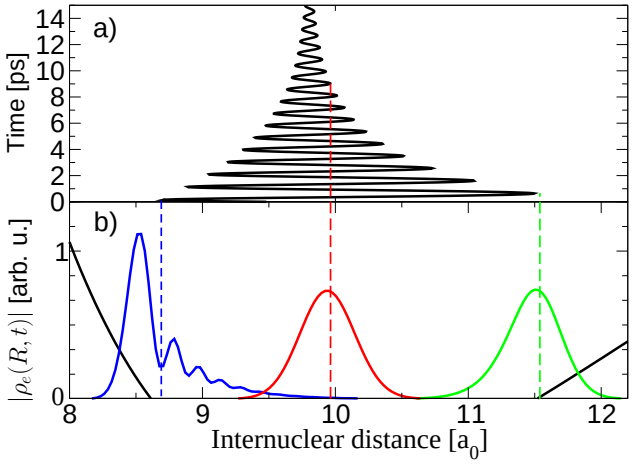

FIG. 3. (a) Temporal oszillation of spatial expectation value for a relaxation rate $\gamma_{\Sigma g} = 0.5\,\mathrm{ps}^{-1}$, (b) Potential energy and density matrix in coordinate space at different time steps.

B. Wave packet dynamics with dissipation

The previous discussion was devoted to isolated vibrating diatomic molecules in the gas-phase. Let us now consider Rb_2 molecules (M) coupled to the dissipative environment realized by helium nanodroplets (HND), to which the molecules are attached. This situation is illustrated in Fig. 3. Snapshots of the WP at characteristic times are shown in Fig. 3 (b) (colored lines), along with the potential curve of the $1^3\Sigma_g^+$-state of Rb_2 (black line). Due to the anharmonicity of the potential, the WP close to the inner and outer turning points are quite different in shape (green and blue lines). After many WP oscillations, the WP has nearly relaxed down to the vibrational ground state ($v = 0$) as a consequence of the dissipative interaction with the surrounding helium. The expectation value of the internuclear distance, $\langle R \rangle$, shown in Fig. 3 (a), consequently oscillates with a decreasing amplitude and eventually reaches the equilibrium distance R_e of the molecule in the vibrational ground state. This scenario corresponds to the WP dynamics in the $1^3\Sigma_g^+$-state excited by a fs-laser at wave length $\lambda = 970\,\mathrm{nm}$, where the system-bath coupling is very efficient and relaxation is fast ($\gamma_{\Sigma g} = 0.5\,\mathrm{ps}^{-1}$).

A Rb_2 molecule attached to a HND is a closed but complicated system which can be described by the hamiltonian $H = H_{\mathrm{M}} + H_{\mathrm{HND}} + H_{\mathrm{M}\leftrightarrow\mathrm{HND}}$. H_{M} denotes the isolated molecule as discussed before, H_{HND} is the hamiltonian for the pure helium nanodroplet and $H_{\mathrm{M}\leftrightarrow\mathrm{HND}}$ contains the interaction between the two. As we are only

interested in the dynamics of the molecule we call this our "system" and the helium nanodroplet our "bath". In our experiments the WP dynamics of the coupled Rb_2 molecule is mostly very similar to that in the gas phase, which means that we see the same fast oscillations, WP dispersion with time constant $T_{\rm disp}$, and (fractional) revivals at times $T_{\rm rev}$. However, on the long time scale of the experiment (nanoseconds) the oscillatory signal exponentially decays due to slow system decoherence. Thus, a description in terms of a weak system-environment coupling is justified.

In the experiment, we observe a decay of the revival amplitudes with the dephasing time constant T_D. This decay is related to the environment-induced decoherence of the WP characterized by T_2. Decoherence can also be caused by pure dephasing which affects only the off-diagonal elements of the density matrix and proceeds on the time scale determined by T_*. Alternatively, vibrational relaxation due to energy dissipation associated with the time scale T_1 also induces loss of coherence. Energy dissipation affects both populations (diagonal elements in the density matrix) and coherences between the populated states (off-diagnonal elements). For the well-known two-level system, the overall decoherence time constant T_2 is related to T_1 and T_* by $1/T_2 = 1/(2\,T_1)+1/T_*$. For multi-level oscillators, which we consider here, the relation between decoherence and dissipation is more subtle. No simple general expression connecting the corresponding time scales exists: depending on the shape of the WP, decoherence may take place on a much shorter time scale [58–61]. We recall that it is important to distinguish between contrast decay due to decoherence – which is an irreversible process – and the reversible drop of the observed oscillation amplitude due to dispersion in an anharmonic potential.

The dissipative vibrational dynamics is described using the framework of Markovian master equations. At this stage, we do not aim at deriving such an equation from a microscopic Hamiltonian, which would require detailed knowledge of the helium "bath" and interaction Hamiltonians $H_{\rm HND}, H_{\rm M\leftrightarrow HND}$. Instead, we choose a well-established Markovian quantum optical master equation [62] for a weakly coupled environment. The density operator $\hat\rho(t)$ of the (reduced) system that describes dissipation in near-harmonic systems at zero temperature is given by

$$\partial_t\hat\rho = \frac{1}{i\hbar}\left[\hat H_M,\hat\rho\right] + \underbrace{\sum_j\left(\hat L_j\hat\rho\hat L_j^\dagger - \frac{1}{2}\{\hat L_j^\dagger\hat L_j,\hat\rho\}\right)}_{\text{coupling to bath}}. \quad (4)$$

This equation is of Lindblad form [63]. To describe dissipation, we use $L_i = \sqrt{\gamma_i}\hat a_i$, where $\hat a_i$ is the usual quantum mechanical ladder operator, defined through the harmonically approximated potential energy curve i. This Lindblad operator induces vibrational dissipation on the time scale $1/\gamma_i$. More specifically, independently of the initial conditions, to good approximation, the mean energy of the excited WP decreases exponentially with a respective rate γ_i. For a single harmonic molecular potential ($H_M = \hbar\omega_e a^\dagger a$), Eq. (4) takes the form

$$\partial_t\hat\rho_{nm} = -i\omega_{nm}\hat\rho_{nm} + \gamma_i\left(\sqrt{n+1}\sqrt{m+1}\hat\rho_{n+1,m+1} - (n+m)\hat\rho_{nm}/2\right), \quad (5)$$

where ω_{nm} are the Bohr frequencies. As time evolves, populations $\hat\rho_{nn}$ are redistributed and at times $t \gtrsim 1/\gamma_i$ mostly the ground state remains occupied. Likewise, the coherences $|\hat\rho_{nm\neq n}|$ decline, which means that the coherent superposition between distinct vibrational states is destroyed. Note that the population of an individual vibrational level may decay much faster than $1/\gamma_i$. If initially only one single excited level $|n\rangle$ is populated, the population decay of this level is $n\gamma_i$. Also decoherence occurs faster than dissipation [64]. However, the exact time scale of decoherence depends on the state $\rho_e(t)$. For a Morse potential, the time-dependent density matrix and in particular the evolution of coherences can be calculated by numerically solving Eq. (4). The relaxation rate constants γ_i in Eq. (4) are taken as fit parameters to match the experimental data.

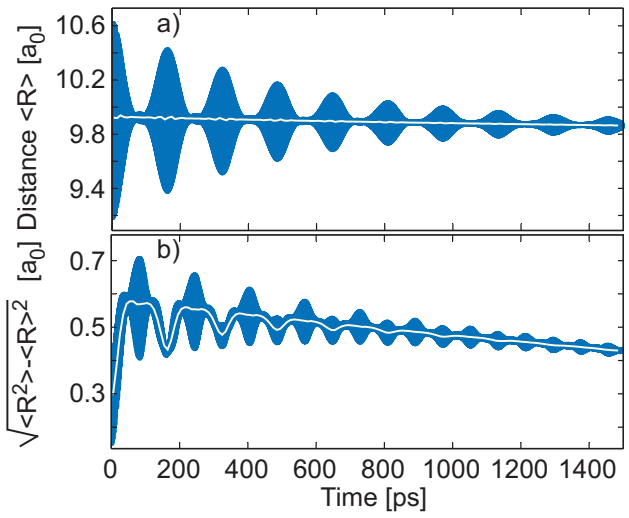

FIG. 4. (a) Expectation value of the internuclear distance $\langle R\rangle$ and (b) standard deviation $\sqrt{\langle R^2\rangle - \langle R\rangle^2}$ of vibrational wave packets in Rb_2 excited by a laser pulse at $\lambda = 1025\,$nm.

A typical model calculation matching experimental parameters ($\lambda = 1025\,$nm) is shown in Fig. 4. At this excitation energy damping is very weak ($\gamma_{\Sigma_g} = 0.36\,\mathrm{ns}^{-1}$) and WP oscillations are visible up to delay times $t \gtrsim 1\,$ns. The expectation value of the internuclear distance (Fig. 4 (a)) oscillates at high frequency with an amplitude that is modulated by WP recurrences (filled area in Fig. 4 (a)). In addition, the time-averaged value (white line) slightly decreases, which reflects slow relaxation into more deeply bound v-states that have shorter internuclear distances. The spatial spread (standard deviation)

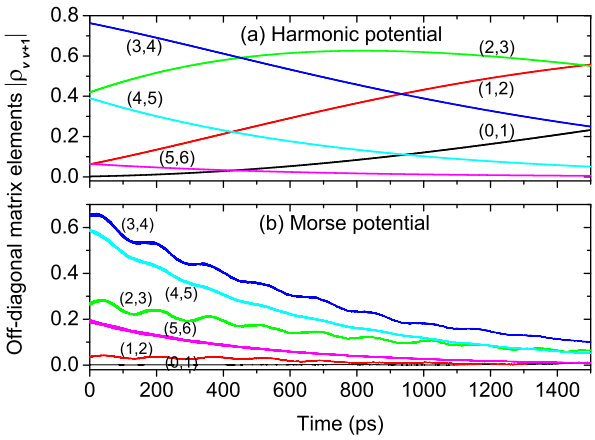

FIG. 5. (Color online) First-order coherences (absolute values of the off-diagonal elements of the density matrix, $\rho_{v\,v+1}$), $v = 0$–6, for vibrational wave packet dynamics in the $1^3\Sigma_g^+$-state potential of Rb_2 (b) in comparison with the harmonically approximated potential (a).

of the WP is particularly small at full revivals of the WP into well-localized nearly coherent states at times $k \times T_{\rm rev}/2 \approx 160,\, 320,\, 480, \ldots$ ps, whereas at pure half-period revivals ($k \times T_{\rm rev}/2 \approx 80,\, 240,\, 400, \ldots$ ps) the WP is maximally delocalized (Fig. 4 (b)).

The chosen dissipative Lindblad operator in Eq. 4 also affects the off-diagonal elements of the density matrix. The latter decay with time due to decoherence which implies a transition from an initially pure state to a state mixture. For $t \to \infty$, only the ground vibrational state is occupied, which is, of course, a pure state again. For the master equation (4) it is well known that localized WPs are "robust" in the sense that they suffer only little decoherence. In contrast, two such WPs separated by a (dimensionless) distance D in phase-space loose their coherence with an accelerated rate $D^2\gamma$ [65–67].

This effect is visualized in Fig. 5, in which the time evolution of the first-order coherences $|\hat{\rho}_{vv+1}|$ of the dynamics in the Morse-type potential of the $1^3\Sigma_g^+$-state of Rb_2 (b) is compared with the dynamics in the harmonically approximated potential (a). The shown initial distribution of coherences is obtained when exciting a WP formed of vibrations $v \approx 0$–6 as observed in the experiment at a laser wave length $\lambda = 1025$ nm. The matrix elements $\hat{\rho}_{vv'}$ are computed by solving Eq. (4) numerically and by projecting onto the eigenstates $|v\rangle$ at every time step. In the case of a harmonic potential (Fig. 5 (a)), beatings between low-lying levels $n \lesssim 3$ initially rise on the shown time scale, whereas the high-lying level beatings monotonically fall to zero. This is due to the vibrational redistribution from the high-lying levels into the lower-lying ones, which evidently not only redistributes population but also transfers coherence from the high-lying to the lower-lying levels.

In the case of the Morse-type potential (Fig. 5 (b)), this tendency is much less pronounced. All the shown coherence terms drop down with slightly varying decay rates. The slower decay of the low-level beatings $(1, 2)$ and $(2, 3)$ in contrast to the faster decay of $(3, 4)$ and $(4, 5)$ is partly reminiscent of the vibrational redistribution mentioned before. In addition, higher excited levels decay faster, see Eq. (5). Thus, for the Morse oscillator the overall decoherence appears to be accelerated with respect to the harmonic oscillator. Moreover, beatings $(2, 3)$ and $(3, 4)$ in Fig. 5 (b) are periodically modulated with period $T_{\rm rev}/2$. In particular, a slow loss of coherence or even a momentary increase of coherence is apparent at times close to the full vibrational recurrences when the WP is reconstituted as a well-localized nearly coherent state. Around the half-period fractional revivals, when the WP splits into partial WPs that are maximally delocalized (large D), however, decoherence is fastest.

C. Numerical simulation

In order to reproduce the ion yield in the gas phase, we calculate the final state probability after the interaction with the laser field. For the isolated dimer, we here follow the approach of [68] and fully numerically solve the describing time dependent Schrödinger equation

$$\partial_t |\Psi(t)\rangle = -\frac{i}{\hbar} H_{\rm M} |\Psi(t)\rangle \qquad (6)$$

for the full state vector $\Psi = (\psi_g, \psi_e, \ldots)$. The Hamilton operator $H_{\rm M}$ now also contains the field interaction with the molecule. In particular, we take into account that the final state consists of the bound ion plus an ejected electron with energy E. Following the approach of [69], we use a discretization of the electronic continuum. We determine the final state probability $|\psi_f(E, \tau)|^2$ for different pump-probe delays τ and electronic energies E. Adding contributions with different energies E, we obtain a signal $S(\tau)$, which is proportional to the gas phase ion yield. For the isolated molecule, Eq. (6) also directly allows to obtain the density operator through $\hat{\rho}(t) = |\Psi(t)\rangle\langle\Psi(t)|$. Potential energy surfaces and transition dipole moments were provided by O. Dulieu [70].

For our phenomenological description of the helium influence on the dimer dynamics, we switch to the density matrix description, Eq. (4). Our aim is to ascribe certain damping parameter values $\gamma_i(\lambda)$ to the measured pump-probe signal at wave lengths λ. From a numerical point of view, the evolution of the density matrix can become very costly, in particular, if one considers many potential energy surfaces and/or many vibrational states. We therefore return to an equation for the state vector, *i. e.* to a Schrödinger-type equation. However, since a deterministic equation can never transform a pure state into a state mixture, one has to involve a stochastic element. Only through the stochastic part in the equation, a stochastic Schrödinger equation (SSE) becomes

equivalent to the density matrix description. The master equation can be recovered from the SSE through an averaging process [71]. In practice, one has to determine many realizations of state vectors $\Psi_{\mathrm{SSE},i}$, which can then be used to extract the density matrix (Fig. 5), coordinate, momentum, energy expectation values (Fig. 4), or the final state probability (Fig. 1 (b)) to compare with the experiment.

III. PUMP-PROBE SPECTRA

Upon laser excitation of Rb_2 molecules formed on helium nanodroplets at wave lengths in the range $\lambda = 960\,\mathrm{nm} - 1032\,\mathrm{nm}$, coherent vibrational WPs are created in the first excited triplet state $1^3\Sigma_g^+$ as well as in the lowest triplet state $a^3\Sigma_u^+$ by RISRS with varying relative intensity. Around $\lambda = 1010\,\mathrm{nm}$, the pump-probe signal as shown in Fig. 1 (a) is dominated by WP motion in the $1^3\Sigma_g^+$-state. The amplitude modulation results from dispersion of the WPs and half-period as well as full recurrences are observed with high contrast at revival times $T_{\mathrm{rev}}/4 \approx 80\,\mathrm{ps}$ and $T_{\mathrm{rev}}/2 \approx 160\,\mathrm{ps}$, respectively. The nearly exponential decrease of the signal contrast is attributed to relaxation-induced decoherence and will be investigated in detail in the following. The simulated transient ($\gamma_{\Sigma g} = 0.45\,\mathrm{ns}^{-1}$), depicted in Fig. 1 (b), nicely reproduces both the vibrational recurrences as well as the overall damping due to vibrational decoherence.

Note, however, that at short delay times $t \lesssim 50\,\mathrm{ps}$ there are significant deviations between the simulated and experimental transient signals. This additional modulation of the experimental data stems from the dynamics of rotational WPs, which was verified by measurements with varying laser polarizations of the pump and probe pulses [72]. The influence of a thermal initial distribution of rotational levels on vibrational coherences and the ensuing decay of wave packet revivals was studied in [73]. Simulations of the rotational WP propagation in the Rb_2 system feature notable rotational recurrences at half and full rotational periods $T_{\mathrm{rot}}/2 \approx 575\,\mathrm{ps}$ and $T_{\mathrm{rot}} \approx 1150\,\mathrm{ps}$, respectively. However, no such signals are observed in the experimental data, which indicates fast rotational relaxation. This assumption is supported by the fast relaxation rates measured with molecules embedded inside helium nanodroplets [5]. Moreover, the position of the Rb_2 molecules in surface states suggests that rotation is hindered quite severely.

The experimental pump-probe signal of Fig. 1 (a) is analyzed by Fourier transforming the time trace inside a time window of a width of 5 ps and a Gaussian apodization function with full width at half maximum (FWHM) of 2.6 ps that slides across the data (wavelet or spectrogram analysis). This type of analysis provides information about the frequency components that make up the WPs without losing the complete dynamical information. The result for $\lambda = 1006\,\mathrm{nm}$ is displayed in Fig. 6 (a). In this representation, the individual WP oscillations are

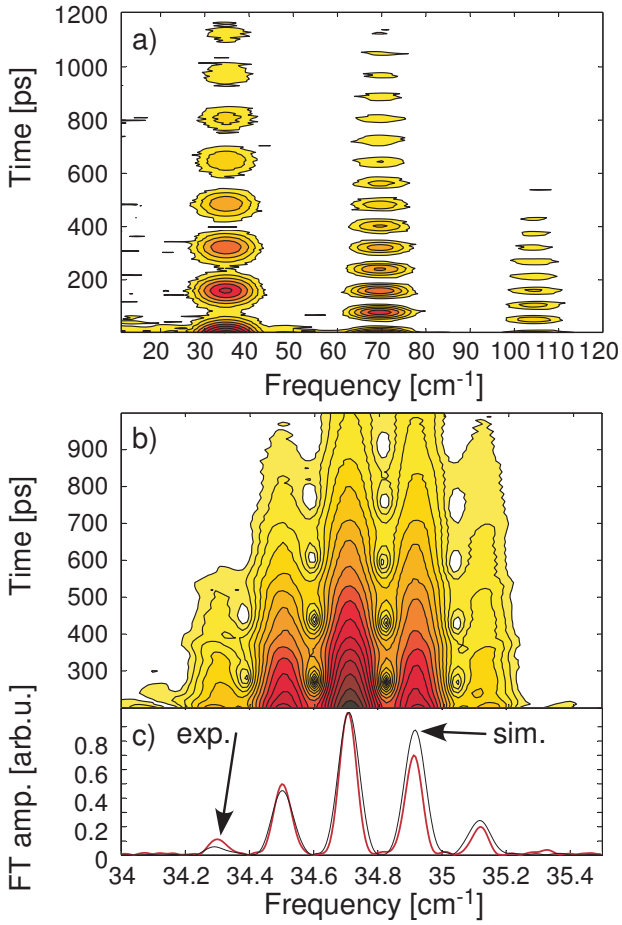

FIG. 6. Sliding window Fourier spectra (spectrograms) of the pump-probe transients recorded at $\lambda = 1006\,\mathrm{nm}$. The width of the time window is 5 ps in (a) and 400 ps in (b). (c) displays the power spectrum of the integral experimental and theoretical transients.

no longer resolved, but the full, half-period and even one third-period revivals are clearly visible and can be attributed to frequency-beatings between vibrational states separated by $\Delta v = 1$, 2, and 3 vibrational quanta, respectively [57]. The fact that the WP recurrences are seen with such an extraordinarily high contrast even at long delay times is a consequence of the shape of the $1^3\Sigma_g^+$-potential that nearly perfectly matches that of the Morse potential [12].

Fig. 6 (b) displays a magnified view of the spectrogram of the same data when using a time window of width 400 ps and an apodization function with FWHM 209 ps in the spectral range $\nu = 34$–$35.5\,\mathrm{cm}^{-1}$. In this representation of the data, the frequency resolution is comparable to the one obtained by transforming the integral data set (Fig. 6 (c)) while still retaining the dynamics on the long time-scale. The individual frequency components reflect beatings between coherently excited adjacent vibrational states that are unequally spaced due to the anharmonicity of the potential. By comparing to the Fourier spectrum of the simulated data in Fig. 6 (c)

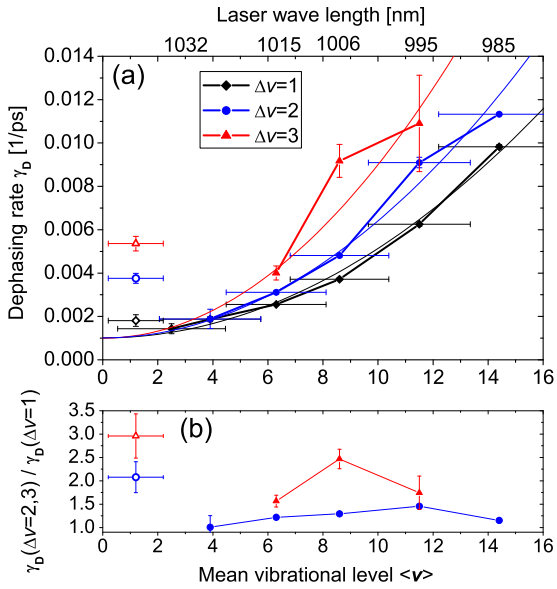

FIG. 7. Exponential decay time constants obtained by fitting the maxima of the full ($\Delta v = 1$) as well as fractional ($\Delta v = 2, 3$) revivals plotted against the average vibrational quantum number of vibrational states initially populated by the pump pulse $\langle v \rangle$. The filled symbols refer to the wave packet dynamics in the excited $1^3\Sigma_g^+$-state, the open symbols refer to the a-state.

we conclude that the WPs excited at $\lambda = 1006\,\mathrm{nm}$ are composed of vibrational states $v = 6$–11 with relative amplitudes determined by the spectral intensity profile of the fs laser.

A. Analysis of decoherence dynamics

In a first attempt to analyze the loss of contrast of the coherent WP oscillation signal the envelopes of the beat signals corresponding to $\Delta v = 1$, 2, 3 are extracted from the spectrograms of the type shown in Fig. 6 (a) at various laser wave lengths. Due to the low spectral resolution the few vibrational beatings that are simultaneously excited according the laser band width are not resolved. Thus, each envelope trace is composed of the sum of individual beatings excited around the central laser wave length. The envelope traces are fitted to an exponential decay function $\propto \exp(-\gamma_\mathrm{D} t)$ to infer the characteristic dephasing rate γ_D.

The fit results for γ_D are depicted in Fig. 7 as a function of the mean vibrational quantum number $\langle v \rangle$ determined by the center laser wave length. The horizontal error bars reflect the width of the distribution of excited vibrational levels due to the laser band width, the vertical error bars depict the fit errors. Strikingly, dephasing is strongly dependent on the level of vibrational excitation and features rapidly increasing dephasing rates γ_D with increasing v. The solid lines in Fig. 7 (a) represent model curves obtained by fitting quadratic functions to the data.

Similar behavior was observed in time-resolved coherent anti-Stokes Raman-scattering measurements of the WP dynamics of molecular iodine I_2 in the groundstate isolated in rare-gas cryo-matrices [33–35]. There, the transition from a linear v-dependence of γ to a quadratic dependence with increasing temperature of the matrix was observed. Linear v-dependence at low temperatures was interpreted in terms of decoherence induced only by vibrational energy relaxation ($1/T_2 \propto 1/T_1$) whereas at higher matrix temperatures pure elastic dephasing ($1/T_*$) also contributed.

Coherences between vibrational states spaced by $\Delta v = n > 1$ are clearly subject to enhanced decay (Fig. 7 (a)). The experimental relative dephasing times amount to $\gamma_\mathrm{D}^{\Delta v=2}/\gamma_\mathrm{D}^{\Delta v=1} \approx 1.3$ and $\gamma_\mathrm{D}^{\Delta v=3}/\gamma_\mathrm{D}^{\Delta v=1} \approx 2$ as shown in Fig.7 (b). The scaling behavior of these multi-order dephasing rates $\gamma_\mathrm{D}^{\Delta v=n}$ with the order n of the beating has been discussed in the context of different mechanisms of pure dephasing [46]. Depending on the collision model considered in that study, a scaling behavior ranging from zeroth to second order with n was expected. Our approach would require the inclusion of pure dephasing terms to account for Δv-dependent dephasing times whereas in the pure relaxation model dephasing times are found to be independent of Δv.

The open symbols in Fig. 7 depict dephasing rate constants γ_D^a for the WP dynamics in the lowest triplet $a^3\Sigma_u^+$-state. While γ_D^a of the first order coherence ($\Delta v = 1$) is similar to those of the excited $1^3\Sigma_g^+$-state for small $\langle v \rangle$, γ_D^a for the higher order coherences are significantly higher than for the $1^3\Sigma_g^+$-state dynamics at low $\langle v \rangle$. This result is reproduced by the simulation based on pure vibrational relaxation and does not necessarily imply pure dephasing in this case. Note, that the initial distribution of v-state populations in the a-state is very different from that in the $1^3\Sigma_g^+$-state. While in the $1^3\Sigma_g^+$-state several v-levels are populated with similar intensities, in the a-state the population is peaked at $v = 0$ and higher v-levels are much less populated by RISRS. Therefore, the γ_D^a values to good approximation reflect dephasing rates between individual v-levels, since redistribution from higher-lying levels is insignificant and the beating signal of n-th order coherence is mainly composed of just one beat frequency.

As we will see later, in the present case of Rb_2 coupled to helium nanodroplets, vibrational relaxation is likely to be the main source of decoherence. Yet, pure dephasing without population transfer does contribute to some extent. In a more complete description both dissipation-induced as well as additional pure dephasing terms should be included to account for the observed v- and Δv-dependences. For the sake of restricting the model to the essential features of the problem, however, in the following discussion we focus on the model calculations that are based on pure vibrational relaxation.

B. Numerical simulation

In order to obtain a more quantitative description of the observed dynamics, the experimental data are modeled using the method outlined in Sec. II C. The only adjustable parameters entering into the simulation are the energy relaxation constants in the triplet ground and first excited states, $\gamma_a = 1/T_1^a$ and $\gamma_{\Sigma g} = 1/T_1^{\Sigma g}$, respectively, as well as relaxation constants for the two probe states $3^3\Pi_u$ and $4^3\Sigma_u^+$. The resulting spectrograms of the best fits to the experimental data are displayed in Fig. 8 (bottom row) for the selected laser wave lengths $\lambda = 1025$, 1006, and 970 nm. For comparison, the top row depicts the experimental data and the middle row shows the simulation when relaxation is absent ($\gamma_a = \gamma_{\Sigma g} = 0$).

The transient recorded at $\lambda = 1006$ nm (center column in Fig. 8), already shown in Fig. 6, is dominated by the fundamental as well as by the first and second overtone beatings of the $1^3\Sigma_g^+$-state. The experimental data (Fig. 8 (d)) are very well reproduced by the numerical simulation for a damping constant $\gamma_{\Sigma g} = 0.45\,\mathrm{ns}^{-1}$ (Fig. 8 (f)), whereas the agreement is clearly worse when no damping is assumed (Fig. 8 (e)). At laser wave lengths $\lambda = 1025$ nm and $\lambda = 970$ nm, WP oscillations in both ground $a^3\Sigma_u^+$ and excited states $1^3\Sigma_g^+$ are present. At $\lambda = 1025$ nm, the excited state-dynamics clearly fades away more slowly than at $\lambda = 1006$ nm, which is in agreement with the simulated data when setting $\gamma_{\Sigma g}$=0.36 ns^{-1} (Fig. 8 (c)). In contrast to the $1^3\Sigma_g^+$-state WP-dynamics, the a-state beatings feature less visible dispersion and recurrences of the WP motion. This is due to the fact that predominantly the vibrational ground-state $v = 0$ is populated by RISRS. Consequently, the fundamental spectral component $\omega_a \approx 13\,\mathrm{cm}^{-1}$ is mainly composed of the beat frequency $(E_{v=1} - E_{v=0})/(h\,c)$, with little contributions of $(E_{v=2} - E_{v=1})/(h\,c)$ and higher level beatings [12]. Best agreement with the experimental data is obtained for $\gamma_a = 3\,\mathrm{ns}^{-1}$ (Fig. 8 (c)). When no damping is assumed, the simulation clearly severely deviates from the experimental data (Fig. 8 (b)). We attribute the additional spectral features to the dynamics in the higher-lying electronic state $3^3\Pi_u$ which has a similarly shaped potential curve as the $1^3\Sigma_g^+$-state. In all simulations including vibrational relaxation, the damping constants of the $3^3\Pi_u$ and of the $4^3\Sigma_u^+$-states are set to $0.1\,\mathrm{ps}^{-1}$ to achieve fast damping of the corresponding WP dynamics, no direct WP signal related to these states is observed in the experiment. However, the inclusion of the two states is crucial in order to reproduce the experimentally observed WP signals in the a-state. The excited state dynamics at $\lambda = 970$ nm is only visible in the time range 0 – 20 ps, after which the a-state dynamics prevails. This behavior is reasonably well reproduced by the simulation when assuming very fast relaxation ($\gamma_{\Sigma g} = 0.5\,\mathrm{ps}^{-1}$, Fig. 8 (i)). In contrast, the same simulation with $\gamma_{\Sigma g} = 0$ shows a dominant contribution of the excited $1^3\Sigma_g^+$-state dynamics (Fig. 8 (h)). At $\lambda = 980$ nm (not shown in Fig. 8), $1^3\Sigma_g^+$-state components are still visible during delay times 0 – 100 ps, which implies fast relaxation at a rate $\gamma_{\Sigma g} = 0.01\,\mathrm{ps}^{-1}$.

An even more detailed verification of the numerical model is achieved by comparing the experimental and theoretical data in the spectrogram representation using a long time window of width 400 ps, as shown in Fig. 6 (b). The high spectral resolution retained in this analysis allows to compare the time evolution of individual beatings between adjacent vibrational states. The amplitudes of individual frequency components are extracted from vertical cuts through the spectrograms at maximum positions and are plotted in Fig. 9 for $\lambda = 1025$ nm. Panels Fig. 9 (a) and (b) represent the experimental data, where in (b) each amplitude component is normalized to the sum of all contributing beat amplitudes. Although all of the frequency components except the lowest one ($v = 0$, $v = 1$) decay in absolute amplitude (Fig. 9 (a)), the relative amplitudes only decrease in the case of the high-lying level beatings (4, 5) and (5, 6), whereas the lower beats (3, 4) remain constant or even rise [(0, 1), (1, 2), and (2, 3)] in amplitude in proportion to the sum of all. The numerical simulations (Fig. 9 (c) and (d)) show the evolution of the first-order coherences of the density matrix. The good agreement highlights the possibility of extracting information about the density matrix by appropriately analyzing the measured ion yields. The general decay and oscillatory behavior of individual beatings is well reproduced by the numerical simulation except for the (0, 1)-beat which is extraordinarily prominent in the experimental data. A slight increase of the absolute beat amplitude of the (0, 1)-component can only be explained by a redistribution of population of higher-lying vibrational levels into lower-lying ones. The weak periodic modulations of both experimental and theoretical curves are reminiscent of the revival structure that becomes more pronounced as the Fourier time window is reduced. The different decay rates for the individual vibrational beatings have been discussed in terms of vibrational redistribution in the harmonic and anharmonic oscillators, (Sec. II B and Fig. 5).

To summarize the results of this detailed analysis the individual frequency components as shown in Fig. 9 excited at various laser wave lengths are fitted by the exponential function $\propto \exp(-\gamma_{\mathrm{D}1} t)$. The resulting values for the fit parameter $\gamma_{\mathrm{D}1}$ are displayed in Fig. 10 for all wave lengths and all detectable beating components with $\Delta v = 1$.

First of all, it is clear that higher beatings decay faster. This has already been shown in Fig. 7 and is also predicted by Eq. (4). Note, however, that decay constants of the same beat frequency components measured at different center wave lengths of the laser systematically increase as the laser is tuned up in wave length and down in terms of the vibrational levels it addresses. Thus, the decoherence rate for a particular beating component $(v, v+1)$ appears to be dependent on the initial distribution of population in neighboring levels. This result is consistent with our model which links decoherence with

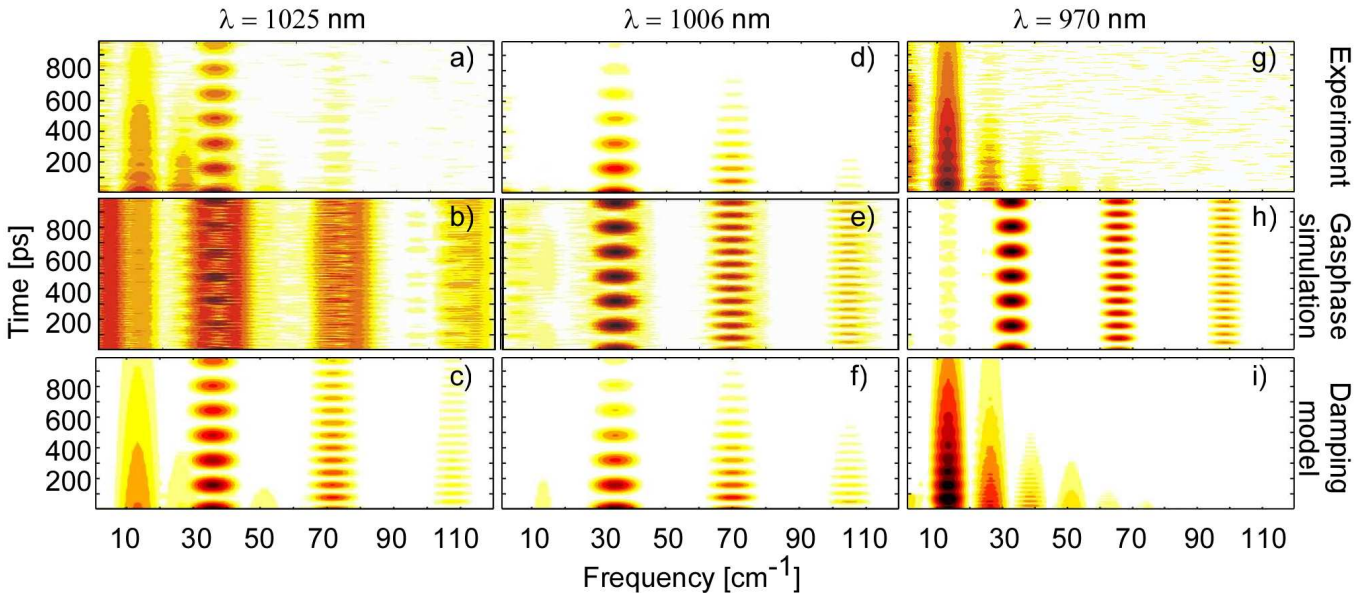

FIG. 8. Comparison between experimental (top row) and theoretical (middle and bottom row) data in spectrogram representation at selected laser wave lengths; The middle row shows the simulation of undamped vibration without coupling to the helium droplets; The bottom row shows the simulation including damping.

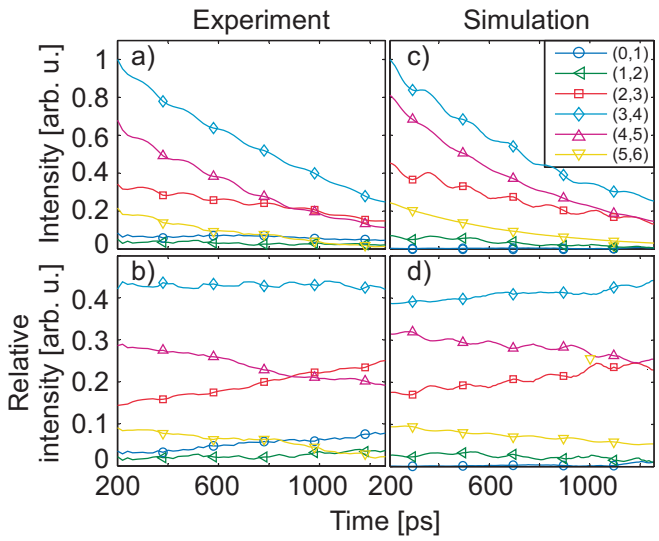

FIG. 9. Time evolution of individual beatings between adjacent vibrational levels ($\Delta v = 1$) of the $1^3\Sigma_g^+$-state extracted from spectrogram analysis of the transient at $\lambda = 1025$ nm with a 400 ps-time window ((a) and (b)) in comparison with simulated density matrix elements $|\rho_{vv+1}|$ ((c) and (d)). Plots (b) and (d) show the same data as (a) and (b) where the beatings are normalized to the sum of all beatings at each time step.

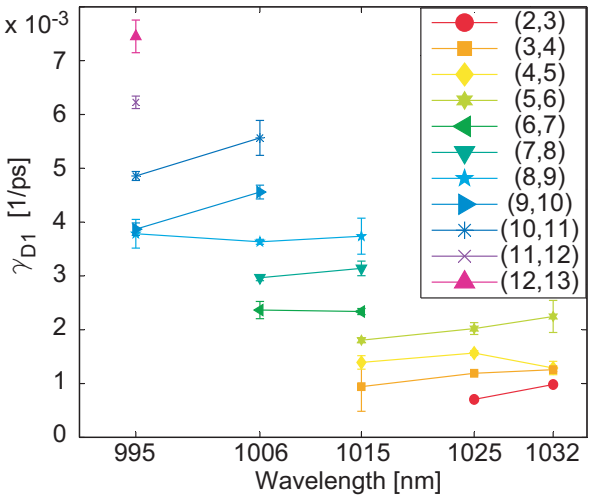

FIG. 10. Exponential decay time constants for individual beatings at various excitation laser wave lengths obtained by fitting the experimental data.

vibrational relaxation, for the following reasons. Consider v to be the lowest level that falls into the spectral laser profile. In this case, both depletion of population and coherence due to relaxation into lower-lying levels as well as enhancement due to the decay of the higher-lying levels into v are active (the last 2 terms on the r.h.s. of Eq. 5 for the case of the harmonic oscillator). Thus, the resulting decay of coherence is delayed. In contrast, if v is the highest level falling into the laser profile, fast decoherence will occur since no replenishing from higher-lying levels is possible. If our model were based on pure decoherence, however, the decay rate of a given beating $(v, v+1)$ would be independent of the population of neighboring vibrational levels.

Since all of the beatings are subject to decoherence the vibrational redistribution is masked by an overall decay

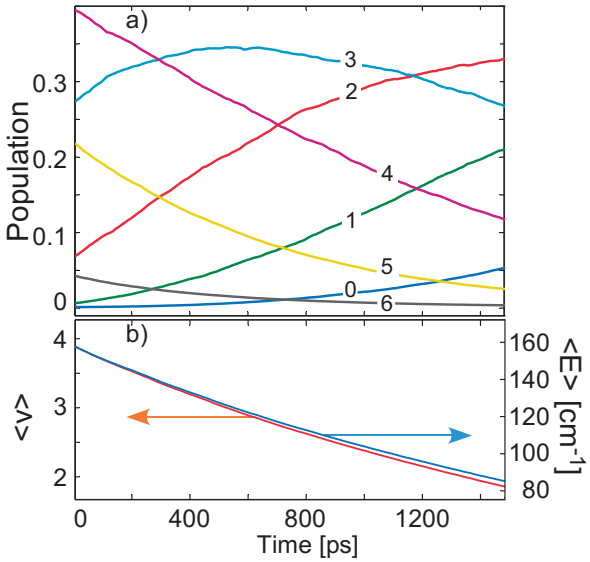

FIG. 11. (a) Time evolution of the populations of individual vibrational states extracted from the simulation at $\lambda = 1025\,\mathrm{nm}$. (b) Evolution of the vibrational level v populated on average and of the mean vibrational energy $\langle E_v \rangle$.

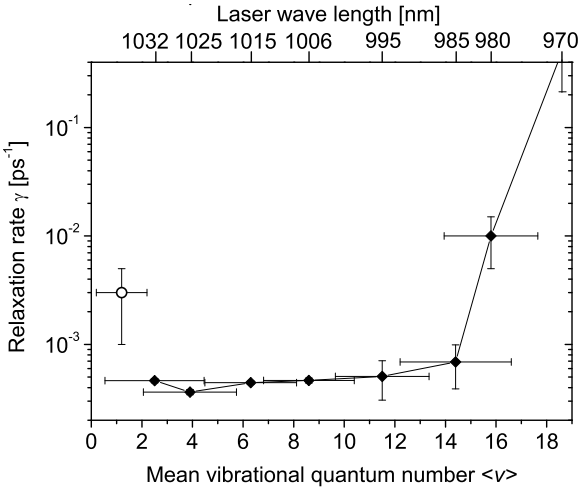

FIG. 12. Dependence of the damping parameter obtained from fitting the simulation to the experimental data as a function of the average vibrational level populated at different laser wave lengths. Filled and open symbols refer to the $1^3\Sigma_g^+$- and the a-states, respectively.

in the representation of absolute amplitudes in Fig. 6 (a) and (c). However, from the simulation we can extract information about the evolution of populations of the individual vibrational states. To this end, the diagonal elements of the density matrix are computed for each time step by projecting the wave function onto the vibrational eigenfunctions. The resulting populations of levels $v = 0$ – 6 are depicted in Fig. 11 (a). Fig. 11 (b) shows the time evolution of the quantum number of the vibrational state that is populated on average as well as the corresponding average vibrational energy. Accordingly, at $\lambda = 1025\,\mathrm{nm}$ the vibrational populations relax down by about 1.8 vibrational quanta during 1.5 ns. The corresponding vibrational energy is reduced by about $E_{\mathrm{diss}} = 73\,\mathrm{cm}^{-1}$. Note that at shorter wave lengths the amount of deposited vibrational energy into the droplets in this time interval is considerably larger, *e. g.* $E_{\mathrm{diss}} = 157\,\mathrm{cm}^{-1}$ at $\lambda = 1006\,\mathrm{nm}$ and $E_{\mathrm{diss}} = 656\,\mathrm{cm}^{-1}$ at $\lambda = 970\,\mathrm{nm}$.

At such high rates of energy transfer to the helium droplets one has to consider the droplet response in terms of heating, superfluidity and cooling by evaporation of helium atoms. From estimates of the excitation energy carried by the droplets as a function of droplet temperature [74] we obtain a rise in temperature from 0.38 K up to $\sim 2.5\,\mathrm{K}$ when $E_{\mathrm{diss}} = 656\,\mathrm{cm}^{-1}$ is deposited into a helium droplet containing 10^4 atoms. This value exceeds the transition temperature to the superfluid phase of bulk helium (2.17 K). Smaller helium droplets heat up to even higher temperatures that may even exceed the boiling temperature of bulk helium. Note, however, that cooling of the droplets due to evaporation of helium atoms may counteract the heating process. In the considered energy range, effective cooling is expected to set in on a time scale of $\sim 100\,\mathrm{ps}$ [74]. Thus, slow energy transfer from the molecules to the droplets at excitations to low-lying v-levels could be partly compensated by evaporation of helium atoms ($E_{\mathrm{diss}} \approx -5\,\mathrm{cm}^{-1}$ per evaporated atom), whereas fast energy transfer may lead to effective heating, to subsequent local disequilibrium states and even to the breakdown of superfluidity. However, after the time of flight of the droplets to the beam depletion detector ($\sim 1\,\mathrm{ms}$) the complete vibrational excitation energy will be transferred to the droplets leading to massive evaporation of up to 150 helium atoms. Thus, the observed beam depletion signal could be due to the deviation of the evaporating droplets out of the beam axis instead of being the result of desorption of Rb_2 from the droplets, as assumed previously.

Having established the observed decay of vibrational beatings in terms of relaxation-induced decoherence using our numerical simulation, let us finally discuss the relaxation time-constants γ_i obtained by fitting the model to the experimental data. Fig. 12 shows γ_a and $\gamma_{\Sigma g}$ as a function of the average vibrational quantum number corresponding to WPs created at different laser wave lengths (top scale). Interestingly, in the range $v = 2$ – 14 the damping parameter remains nearly constant, $\gamma_{\Sigma g} \approx 0.5\,\mathrm{ns}^{-1}$, even though significantly varying dephasing time-constants γ_{D} have been measured (Fig. 7). This discrepancy reflects the scaling behavior of decoherence times with v, as discussed in Sec. II B. The nearly v-independent values of $\gamma_{\Sigma g}$ are quite unexpected considering various model predictions of strongly v-dependent

relaxation rates [38, 43, 75]. At higher vibrational excitations $v \gtrsim 15$, though, the experimental data can only be modeled when assuming drastically increased values of $\gamma_{\Sigma g}$. The ground state relaxation rate γ_a (open symbol in Fig.12) is found to be higher by about a factor 6 as compared to the excited state rate $\gamma_{\Sigma g}$.

The sharp rise of $\gamma_{\Sigma g}$ at $\langle v \rangle \gtrsim 15$ could be related to the breakdown of superfluidity or even the effect of a liquid to gas phase transition in the helium droplets due to fast heating. Alternatively, new coupling channels, *e. g.* the excitation of collective modes of the helium droplets that may be related to their superfluid character (*i. e.* rotons) may also be at the origin of increasing relaxation rates [25]. At this stage, however, this assumption seems unlikely, given the fact that the vibrational energy quanta ($\sim 35\,\mathrm{cm}^{-1}$) largely exceed the elementary excitations of superfluid helium droplets. The ripplon energies are in the range $0.1\,\mathrm{cm}^{-1}$, phonon modes have energies $\sim 1\,\mathrm{cm}^{-1}$, and the roton energy is about $10\,\mathrm{cm}^{-1}$ [74, 76]. Possibly, intra-molecular couplings or more complex excitation pathways leading to the ionic continuum may also be involved.

IV. CONCLUSION

In conclusion, femtosecond pump-probe measurements of the vibrational wave packet dynamics of Rb_2 molecules attached to helium nanodroplets are analyzed using dissipative quantum simulations. In contrast to earlier interpretations, Rb_2 excited to triplet states are found to remain attached to the helium droplets on the time scale of the pump-probe experiments and reveal slow damping of the vibrational wave packet signal due to the interaction with the helium droplet environment. The weak system-bath coupling results in slow damping dynamics compared to the periods of vibration, which is prototypical for the applied master equation. Thus, helium droplets provide a versatile test bed for studying relaxation dynamics and cooling processes induced by a highly quantum environment.

From the detailed comparison of the experimental data in the time- and frequency domains with model calculations it is possible to deduce the evolution of the density matrix describing the vibrating Rb_2 molecules. Good agreement is achieved under the model assumption of vibrational relaxation-induced decoherence with negligible contribution by pure dephasing. We extract damping constants for the vibrational relaxation in the lowest triplet state $a^3\Sigma_u^+$ and in the first excited state $1^3\Sigma_g^+$, $\gamma_a \approx 3\,\mathrm{ns}^{-1}$ and $\gamma_{\Sigma g} \approx 0.5\,\mathrm{ns}^{-1}$, respectively. The pronounced dependence of $\gamma_{\Sigma g}$ on the vibrational quantum number v may be related to the interplay of effective heating of the droplets by fast energy transfer from the molecules and cooling due to evaporation of helium atoms. High heating rates may induce phase transitions in the droplets that affect the dynamics of attached molecules. Thus, this kind of study could open the possibility of probing the fundamental properties and dynamics of helium droplets. Further experiments as well as modeling of the response of the helium droplets to vibronic excitations of embedded atoms and molecules is needed. In particular the dependence of dephasing and relaxation dynamics of the vibrational state quantum number may provide detailed information about the solute-solvant coupling mechanisms and may contribute to interpreting the shapes of spectral lines. Moreover, the dynamics of the desorption process of alkali atoms and molecules off the droplet surface in dependence of the atomic species and the particular vibronic state excited is still mostly unresolved.

ACKNOWLEDGMENTS

We thank G. Stock and F. Mintert for valuable discussions. Support by the Deutsche Forschungsgemeinschaft (DFG) is gratefully acknowledged. Computing resources have been provided by the Zentrum für Informationsdienste und Hochleistungsrechnen (ZIH) at the TU Dresden. M. S. is a member of the IMPRS Dresden.

[1] J. P. Toennies and A. F. Vilesov, Angew. Chem. Int. Ed. **43**, 2622 (2004).
[2] S. Grebenev, J. P. Toennies, and A. F. Vilesov, Science **279**, 2083 (1998).
[3] F. Stienkemeier and K. Lehmann, J. Phys. B **39**, R127 (2006).
[4] K. Nauta and R. E. Miller, J. Chem. Phys. **115**, 45084514 (2001).
[5] C. Callegari, I. Reinhard, K. K. Lehmann, G. Scoles, K. Nauta, and R. E. Miller, J. Chem. Phys. **113**, 4636 (2000).
[6] B. Dick and A. Slenczka, J. Chem. Phys. **115**, 10206 (2001).
[7] R. Lehnig, P. L. Raston, and W. Jäger, Faraday Discuss. **142**, 297 (2009).
[8] O. Bünermann, G. Droppelmann, A. Hernando, R. Mayol, and F. Stienkemeier, J. Phys. Chem. A **111**, 12684 (2007).
[9] K. Nauta and R. E. Miller, J. Chem. Phys. **111**, 3426 (1999).
[10] K. Nauta and R. E. Miller, J. Chem. Phys. **113**, 9466 (2000).
[11] D. T. Moore and R. E. Miller, J. Chem. Phys. **118**, 9629 (2003).
[12] M. Mudrich, P. Heister, T. Hippler, C. Giese, O. Dulieu, and F. Stienkemeier, Phys. Rev. A **80**, 042512 (2009).
[13] M. Koch, G. Auböck, C. Callegari, and W. E. Ernst, Phys. Rev. Lett. **103**, 035302 (2008).

[14] A. Braun and M. Drabbels, Phys. Rev. Lett. **93**, 253401 (2004).
[15] A. Przystawik, S. Göde, T. Döppner, J. Tiggesbäumker, and K.-H. Meiwes-Broer, Phys. Rev. A **78**, 021202 (2008).
[16] O. Kornilov, C. C. Wang, O. Bünermann, A. T. Healy, M. Leonard, C. Peng, S. R. Leone, D. M. Neumark, and O. Gessner, J. Phys. Chem. A **114**, 1437 (2010).
[17] G. Droppelmann, O. Bünermann, C. P. Schulz, and F. Stienkemeier, Phys. Rev. Lett. **93**, 0233402 (2004).
[18] M. Mudrich, G. Droppelmann, P. Claas, C. Schulz, and F. Stienkemeier, Phys. Rev. Lett. **100**, 023401 (2008).
[19] P. Claas, G. Droppelmann, C. P. Schulz, M. Mudrich, and F. Stienkemeier, J. Phys. B **39**, S1151 (2006).
[20] P. Claas, G. Droppelmann, C. P. Schulz, M. Mudrich, and F. Stienkemeier, J. Phys. Chem. A **111**, 7537 (2007).
[21] R. Mayol, F. Ancilotto, M. Barranco, O. Bünermann, M. Pi, and F. Stienkemeier, J. Low Temp. Phys. **138**, 229 (2005).
[22] F. Dalfovo, Z. Phys. D **29**, 61 (1994).
[23] F. Ancilotto, G. DeToffol, and F. Toigo, Phys. Rev. B **52**, 16125 (1995).
[24] F. Stienkemeier, J. Higgins, W. E. Ernst, and G. Scoles, Phys. Rev. Lett. **74**, 3592 (1995).
[25] M. Schlesinger, M. Mudrich, F. Stienkemeier, and W. T. Strunz, Chem. Phys. Lett. **490**, 245 (2010).
[26] T. Takayanagi and M. Shiga, Phys. Chem. Chem. Phys. **6**, 3241 (2004).
[27] F. R. Brühl, R. A. Trasca, and W. E. Ernst, J. Chem. Phys. **115**, 10220 (2001).
[28] G. Auböck, J. Nagl, C. Callegari, and W. E. Ernst, Phys. Rev. Lett. **101**, 035301 (2008).
[29] Q. Liu, C. Wan, and A. H. Zewail, J. Phys. Chem. A **100**, 18666 (1996).
[30] V. A. Ermoshin, A. K. Kazansky, and V. Engel, J. Chem. Phys. **111**, 7807 (1999).
[31] C. Meier and J. A. Beswick, J. Chem. Phys. **121**, 4550 (2004).
[32] M. Gühr, M. Bargheer, M. Fushitani, T. Kiljunen, and N. Schwentner, Phys. Chem. Chem. Phys. **9**, 779 (2007).
[33] M. Karavitis, D. Segale, Z. Bihary, M. Pettersson, and V. A. Apkarian, Low Temp. Phys. **29**, 814 (2003).
[34] M. Karavitis and V. A. Apkarian, J. Chem. Phys. **120**, 292 (2004).
[35] T. Kiviniemi, J. Aumanen, P. Myllyperkiö, V. A. Apkarian, and M. Pettersson, J. Chem. Phys. **123**, 064509 (2005).
[36] M. Gühr, H. Ibrahim, and N. Schwentner, Phys. Chem. Chem. Phys. **6**, 5353 (2004).
[37] M. Fushitani, M. Bargheer, M. Gühr, and N. Schwentner, Phys. Chem. Chem. Phys. **7**, 3143 (2005).
[38] E. Bodo, F. A. Gianturco, and E. Yurtsever, Phys. Rev. A **73**, 052715 (2006).
[39] E. Bodo and F. Gianturco, Int. Rev. Phys. Chem. **25**, 313 (2006).
[40] D. Caruso, M. Tacconi, E. Yurtsever, and F. A. Gianturco, Phys. Rev. A **81**, 042710 (2010).
[41] A. H. Zewail and D. J. Diestler, Chem. Phys. Lett. **65**, 37 (1979).
[42] M. Karavitis, T. Kumada, I. U. Goldschleger, and V. A. Apkarian, Phys. Chem. Chem. Phys. **7**, 791 (2005).
[43] A. Nitzan, S. Mukamel, and J. Jortner, J. Chem. Phys. **63**, 200 (1975).
[44] R. Englman, *Non-Radiative Decay of Ions and Molecules in Solids* (North Holland, Amsterdam, 1979).
[45] J. S. Bader, B. J. Berne, E. Pollak, and P. Hänggi, J. Chem. Phys. **104**, 1111 (1996).
[46] E. Gershgoren, Z. Wang, S. Ruhman, J. Vala, and R. Kosloff, J. Chem. Phys. **118**, 3660 (2003).
[47] P. Földi, M. G. Benedict, A. Czirják, and B. Molnár, Fortschr. Phys. **51**, 122 (2003).
[48] J. Chesnoy and A. Mokhtari, Phys. Rev. A **38**, 3566 (1988).
[49] M. Gruebele, G. Roberts, M. Dantus, R. M. Bowman, and A. H. Zewail, Chem. Phys. Lett. **166**, 459 (1990).
[50] V. Engel, Chem. Phys. Lett. **178**, 130 (1991).
[51] M. Seel and W. Domcke, Chem. Phys. **151**, 59 (1991).
[52] M. Seel and W. Domcke, J. Chem. Phys. **95**, 7806 (1991).
[53] S. I. Vetchinkin and V. V. Eryomin, Chem. Phys. Lett. **222**, 394 (1994).
[54] I. S. Averbukh and N. F. Perelman, Phys. Lett. A **139**, 449 (1989).
[55] M. O. Scully and M. S. Zubairy, *Quantum Optics* (Cambridge University Press, 1997).
[56] I. S. Averbukh, M. J. J. Vrakking, D. M. Villeneuve, and A. Stolow, Phys. Rev. Lett. **77**, 3518 (1996).
[57] M. J. J. Vrakking, D. M. Villeneuve, and A. Stolow, Phys. Rev. A **54**, R37 (1996).
[58] E. Joos and H. D. Zeh, Z. Phys. B **59**, 223 (1985).
[59] W. H. Zurek, Physics Today **44**, 36 (1991).
[60] D. Giulini, *Decoherence and the Appearance of a Classical World in Quantum Theory* (Springer, Heidelberg, 1996).
[61] M. Tegmark and J. A. Wheeler, Scientific American (2001).
[62] H. Breuer and F. Petruccione, *The theory of open quantum systems* (Oxford University Press, 2002).
[63] G. Lindblad, Commun. Math. Phys. **40**, 147 (1975).
[64] A. O. Caldeira and A. J. Leggett, Phys. Rev. A **31**, 1059 (1985).
[65] D. F. Waals and G. J. Milburn, Phys. Rev. A **31**, 2403 (1985).
[66] M. Brune, S. Haroche, J. M. Raimond, L. Davidovich, and N. Zagury, Phys. Rev. A **45**, 5193 (1992).
[67] D. Braun, F. Haake, and W. T. Strunz, Phys. Rev. Lett. **86**, 2913 (2001).
[68] R. de Vivie-Riedle, K. Kobe, J. Manz, W. Meyer, B. Reischl, S. Rutz, E. Schreiber, and L. Wöste, J. Phys. Chem. **100**, 7789 (1996).
[69] R. de Vivie-Riedle, B. Reischl, S. Rutz, and E. Schreiber, J. Phys. Chem. **99**, 16829 (1995).
[70] R. Beuc, M. Movre, V. Horvatic, C. Vadla, O. Dulieu, and M. Aymar, Phys. Rev. A **75**, 032512 (2007).
[71] N. Gisin and I. C. Percival, J. Phys. A: Math. Gen. **25**, 5677 (1992).
[72] M. Gruebele and A. H. Zewail, Journal Of Chemical Physics **98**, 883 (1993).
[73] M. Schlesinger and W. T. Strunz, Phys. Rev. A **77**, 012111 (2008).
[74] D. M. Brink and S. Stringari, Z. Phys. D **15**, 257 (1990).
[75] S. A. Egorov and J. L. Skinner, J. Chem. Phys. **105**, 7047 (1996).
[76] S. A. Chin and E. Krotscheck, Phys. Rev. B **52**, 10405 (1995).